



1 **Sensitivity of aerosol and cloud properties to coupling strength of**
2 **marine boundary layer clouds over the northwest Atlantic**

3 Kira Zeider¹, Kayla McCauley²⁺, Sanja Dmitrovic³, Leong Wai Siu², Yonghoon Choi^{4,5}, Ewan C.
4 Crosbie^{4,5}, Joshua P. DiGangi⁴, Glenn S. Diskin⁴, Simon Kirschler^{6,7}, John B. Nowak⁴, Michael
5 A. Shook⁴, Kenneth L. Thornhill^{4,5}, Christiane Voigt^{6,7}, Edward L. Winstead^{4,5}, Luke D. Ziemba⁴,
6 Paquita Zuidema⁸, Armin Sorooshian^{1,2,3*}

7 ¹Department of Chemical and Environmental Engineering, University of Arizona, Tucson, AZ, 85721, USA

8 ²Department of Hydrology and Atmospheric Sciences, University of Arizona, Tucson, AZ, 85721, USA

9 ³James C. Wyant College of Optical Sciences, University of Arizona, Tucson, AZ 85721, USA

10 ⁴NASA Langley Research Center, Hampton, VA, 23681, USA

11 ⁵Analytical Mechanics Associates, Hampton, VA, 23666, USA

12 ⁶Institute of Atmospheric Physics, German Aerospace Center, Germany

13 ⁷Institute of Atmospheric Physics, University Mainz, Germany

14 ⁸Rosenstiel School of Marine, Atmospheric, and Earth Science, University of Miami, Miami, FL

15 ⁺Now at EPA, Research Triangle Park, NC 27711

16

17 **Correspondence to:* Armin Sorooshian (armin@arizona.edu)



18 **Abstract**

19 Quantifying the degree of coupling between marine boundary layer clouds and the surface is critical for understanding
20 the evolution of low clouds and explaining the vertical distribution of aerosols and microphysical cloud properties. In
21 this study, we use aircraft data from the NASA Aerosol Cloud meTeorology Interactions oVer western ATLantic
22 Experiment (ACTIVATE) to assess aerosol and cloud characteristics for the following four regimes of coupling
23 strength as quantified using differences in liquid water potential temperature (θ_l) and total water mixing ratio (q_t)
24 between a near-surface level (~150 m) and directly below cloud bases: strong coupling ($\Delta\theta_l \leq 1.0$ K, $\Delta q_t \leq 0.8$ g kg⁻¹),
25 moderate coupling with high $\Delta\theta_l$ ($\Delta\theta_l > 1.0$ K, $\Delta q_t \leq 0.8$ g kg⁻¹), moderate coupling with high Δq_t ($\Delta\theta_l \leq 1.0$ K, Δq_t
26 > 0.8 g kg⁻¹), weak coupling ($\Delta\theta_l > 1.0$ K, $\Delta q_t > 0.8$ g kg⁻¹). Results show that (i) turbulence is greater in the strong
27 coupling regime compared to the weak coupling regime, with the former corresponding to smaller differences in 550
28 nm aerosol scattering, integrated aerosol volume concentration, and giant aerosol number concentration ($D_p > 3$ μ m)
29 between the near-surface level and just below marine boundary layer (MBL) cloud bases coincident with increased
30 MBL mixing, (ii) cloud drop number concentration is greater during periods of strong coupling due to the greater
31 upward vertical velocity and subsequent activation of particles, (iii) sea-salt tracer species (Na^+ , Cl^- , Mg^{2+} , K^+) are
32 present in greater concentrations in the strong coupling regime compared to weak coupling, while Ca^{2+} , nss-SO_4^{2-} ,
33 NO_3^- , oxalate, and NH_4^+ (tracers of continental pollution) are higher in mass fraction for the weak coupling regime.
34 Additionally, pH and $\text{Cl}^-:\text{Na}^+$ (a marker for chloride depletion) are consistently lower in the weak coupling regime.
35 There were differences between the two moderate regimes: the moderate high Δq_t regime had greater turbulent mixing
36 and sea salt concentrations in cloud water, along with smaller differences in integrated volume and giant aerosol
37 number concentration between the two vertical levels compared. This work shows value in defining multiple coupling
38 regimes (rather than the traditional coupled versus decoupled) and demonstrates differences in aerosol and cloud
39 behavior in the MBL for the various regimes.

40



41 **1 Introduction**

42 The composition of marine boundary layer (MBL) cloud properties is strongly linked to the lower troposphere's
 43 vertical structure, making it critical to understand the degree of coupling between boundary layer clouds and the
 44 ocean's surface. When the MBL is well-mixed, there is a thermodynamic exchange between the ocean's surface and
 45 the cloud deck, and it is considered coupled. A decoupled MBL is characterized by a stable layer separating two well-
 46 mixed layers (the cloud deck and sub-cloud layer), preventing exchange between the ocean's surface and the cloud
 47 base (Nicholls, 1984; Dong et al., 2015; Jones et al., 2011; Wang et al., 2016). Whether the MBL cloud deck is coupled
 48 or decoupled to the surface has potentially important implications for cloud and aerosol properties (Dong et al., 2015;
 49 Wang et al., 2016; Griesche et al., 2021), radiative forcing (Goren et al., 2018), and precipitation (Bretherton et al.,
 50 2010; Dong et al., 2015). Changes in cloud properties and precipitation affect how much solar radiation is reflected to
 51 space (Twomey, 1974; Albrecht, 1989), which in turn affects how much radiative cooling occurs (Ramanathan et al.,
 52 1989).

53

54 Past studies have investigated coupling behavior of marine stratocumulus due to their relatively high frequency over
 55 the ocean's surface and strong impact on the Earth's radiation budget (Zuidema et al., 2009; Jones et al., 2011; Dong
 56 et al., 2015; Wang et al., 2016; Goren et al., 2018). In marine regions, well-mixed moist thermodynamic statistics
 57 indicate coupling of the sub-cloud layer to the surface (Bretherton et al., 1997; Jones et al., 2011; Dong et al., 2015;
 58 Wang et al., 2016; Su et al., 2022). Studies beyond those previously mentioned over the southeast and northeast Pacific
 59 have applied these methods to other regions, such as the Arctic (Griesche et al., 2021) and over land in the Southern
 60 Great Plains of the United States (Su et al., 2022). Table 1 provides a synthesis of previous studies that utilized
 61 thermodynamic statistics for determining coupling, including criteria used, the region in which the study was
 62 conducted, and the cloud types investigated.

63

64 **Table 1: Summary of coupling criteria and regional conditions from previous work in comparison to this study.**

Study region; reference	Criteria	Secondary criteria	Layers used	Cloud type
Southeast Pacific; Jones et al. (2011)	Coupled: $\Delta q_t < 0.5 \text{ g kg}^{-1}$ & $\Delta \theta_t < 0.5 \text{ K}$	Coupled: distance between lifting condensation level (LCL) and cloud base is < 150 m	Bottom 25% of surface layer to cloud base height	Marine strato- cumulus
Azores (Graciosa Island; Northeast Atlantic); Dong et al. (2015)	All other profiles are considered decoupled	Decoupled: distance > 150 m		
Northeast Pacific; Wang et al. (2016)	Decoupled: $\Delta q_t > 0.6 \text{ g kg}^{-1}$ & $\Delta \theta_t > 1.0 \text{ K}$	N/A		
	All other clouds are considered coupled			



Southern Great Plains (U.S.); Su et al. (2022)	Coupled: $\Delta\theta_t < 1.0$ K Decoupled: $\Delta\theta_t > 1.0$ K			Different Thermodynamic Stability (DTDS) method	Cloud base height minus planetary boundary layer height	Low clouds over land, specifically cumulus
Northwest Atlantic; This Study	Degree	Δq_t	$\Delta\theta_t$	N/A	Below cloud base leg (~100 m below base) minus MinAlt leg (avg. alt ~150 m)	Marine clouds spanning continuum from stratiform to cumulus
	Strong	≤ 0.8 g kg ⁻¹	≤ 1.0 K			
	Moderate, high $\Delta\theta_t$	≤ 0.8 g kg ⁻¹	> 1.0 K			
	Moderate, high Δq_t	> 0.8 g kg ⁻¹	≤ 1.0 K			
Weak	> 0.8 g kg ⁻¹	> 1.0 K				

65

66 As over 45% of the ocean’s surface is covered by MBL clouds (Warren et al., 1988), examining relations between
 67 aerosol and cloud characteristics with coupling strength is important. Investigation of coupling behavior has not yet
 68 been carried out for the northwest Atlantic region, which is a complex thermodynamic region for such work as it is
 69 not a classical sub-tropical zone with a stratocumulus cloud deck like most regions investigated in Table 1 (Painemal
 70 et al., 2021, 2023). The synoptic conditions over the northwest Atlantic are such that the wintertime has higher cloud
 71 fraction with more influence from stratiform boundary layer clouds, whereas the summertime has more trans-Atlantic
 72 flow in addition to lower cloud fraction with higher sea surface temperatures promoting shallow cumulus clouds
 73 (Painemal et al., 2021). During winter, there is more offshore advection of continental air (Corral et al., 2021;
 74 Dadashazar et al., 2021), enhanced precipitation frequency (Painemal et al., 2021), and cold air outbreaks (CAOs), in
 75 which cold air is advected across the Gulf Stream front resulting in pronounced differences between air and sea surface
 76 temperatures (Brümmer, 1997; Papritz & Spengler, 2015; Seethala et al., 2021). CAOs are typically associated with
 77 strong turbulent mixing, leading to the deepening of the boundary layer (Dadashazar et al., 2021; Painemal et al.,
 78 2021; Papritz & Spengler, 2015; Tornow et al., 2022). During CAO events, surface wind convergence is driven by
 79 horizontal pressure and boundary layer height gradients, contributing to a statically unstable troposphere (Painemal et
 80 al., 2021; Seethala et al., 2021).

81

82 Motivated by meteorological differences between the northwest Atlantic and other regions in Table 1, the question
 83 arises as to whether it is restrictive to consider just the categories of coupled and decoupled clouds; instead, it may be
 84 instructive to consider more categories and that they all may have some degree of coupling ranging from weak to
 85 strong. This strategy is built off past reports suggesting that the use of the term “decoupled” may not be appropriate
 86 and that an MBL can be coupled even though it is poorly mixed (Stevens et al., 1998). The latter case can be viewed
 87 as weakly coupled due to episodic updraft-driven convection that is less efficient at mixing the MBL than is the case
 88 in well-mixed MBLs in which downdrafts associated with cloud-top radiative cooling couple the cloud and sub-cloud
 89 layers. Thus, the perspective we embrace in this work is that low-level clouds (< 2 km) can be viewed as always being
 90 coupled to sub-cloud layers but to varying degrees.

91



92 The goal of this study is to leverage an opportune aircraft dataset covering multiple seasons between 2020 to 2022
93 from NASA’s Aerosol Cloud meTeorology Interactions oVer the western ATlantic Experiment (ACTIVATE;
94 Sorooshian et al., 2019) to quantify the frequency of occurrence for four different coupling regimes and how aerosol
95 and cloud characteristics vary between them. We emphasize that this study is different in nature to those in Table 1 in
96 that we do not examine as rigorously the vertical extent of the full cloudy boundary layer but instead focus more on
97 aerosol and cloud characteristics for different coupling regimes based on definitions limited to the vertical region
98 below cloud bases. The analyses presented here are important for reasons such as knowing how well the aerosol near
99 the surface level represents the aerosol just below cloud bases, with implications for the aerosol that largely govern
100 the drop concentration budget. In Sect. 2 we summarize the measurements and methods, including criteria applied
101 with traditionally used thermodynamic variables to differentiate between four coupling categories. In Sect. 3 we report
102 results including the frequency of occurrence of the four coupling regimes, and differences in aerosol properties (light
103 scattering, aerosol number/volume) and cloud microphysical properties (composition and drop number concentration)
104 between these categories to see how they compare to past studies for other regions. Although there are scarce previous
105 reports of such findings (e.g., Dong et al., 2015; Wang et al., 2016), the central hypotheses are based on confirming
106 what has been shown in other regions, in that more strongly coupled cases will have: (i) more similar values for aerosol
107 properties in the sub-cloud layer compared to closer to the ocean’s surface; (ii) cloud composition reflecting
108 significantly more sea salt influence; and (iii) higher cloud drop number concentration. Differences identified in
109 aerosol and cloud characteristics between these four coupling regimes are important to inform future research to
110 account for thermodynamic profiles when examining aspects of aerosol and cloud microphysics when using either
111 satellite, reanalysis, airborne, or ground-based datasets.

112

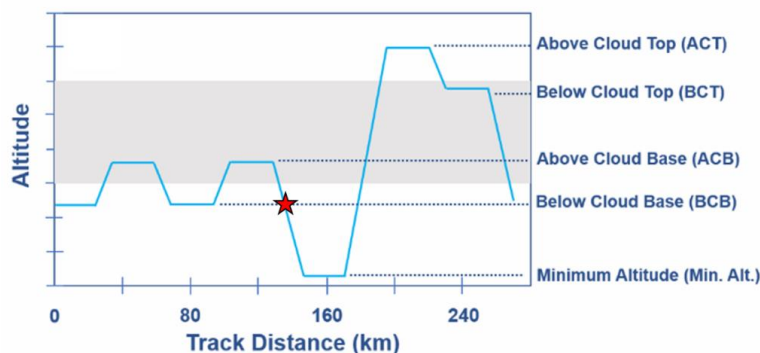
113 **2 Data and Methodology**

114 **2.1 Overview of ACTIVATE**

115 ACTIVATE was largely based out of NASA Langley Research Center in Hampton, Virginia and carried out research
116 flights (RFs) with two spatially coordinated aircraft as part of six deployments in winter and summer months between
117 2020 and 2022, with extensive measurement and deployment details provided elsewhere (Sorooshian et al., 2023).
118 Secondary bases were used for a subset of flights in 2022, including in Bermuda for June 2022. Winter and summer
119 are broadly defined as including the months of November-April and May-September, respectively. The HU-25 Falcon
120 flew level legs in, below, and above the MBL to collect in-situ atmospheric state, aerosol, trace gas, and cloud
121 measurements, while the high-flying King Air at ~9 km launched dropsondes and carried out remote sensing. The
122 focus of this work is data collected by the Falcon. Out of 179 total flights, 135 were used that offered data conducive
123 to this study’s analysis including having the Falcon conduct “statistical survey” flights with “cloud ensembles” (Fig.
124 1), along with several physical conditions satisfied as discussed in Sect. 2.5. During statistical survey flights, which
125 accounted for 93% of ACTIVATE’s flights, the Falcon repeatedly flew a series of legs with Fig. 1 visually depicting
126 one such cloud ensemble whereby the plane flew the following legs in this nominal order: two pairs of legs below
127 cloud base (BCB) and above cloud base (ACB) followed by a descent to the minimum altitude (MinAlt) possible
128 (~150 m above sea level) and then a subsequent slant ascent for a leg above cloud top (ACT) followed by a final leg



129 below cloud top (BCT). Separate ensembles flown in clear air conditions are outside the scope of this work. Each leg
130 duration was ~ 3.3 minutes (equivalent to ~ 24 km) with the Falcon flying at ~ 120 m s⁻¹ (Dadashazar et al., 2022a).
131 The vertical slant ascents/descents between level legs especially down to MinAlt and up to ACT were helpful in
132 gathering vertically-resolved information during ensembles.



133
134 **Figure 1:** Cloudy ensemble flight strategy of the HU-25 Falcon during the ACTIVATE flights, where the grey box represents
135 a typical cloud layer with upper and lower boundaries representing cloud top and base, respectively. The order of legs was
136 the nominal plan that was flown, but sometimes the legs were flown in a different order based on flight restrictions and
137 cloud conditions. The red star indicates where the BCB level would be marked for this particular flight pattern, which is
138 during the slant descent from ACB to MinAlt and uses the mean altitude of the preceding BCB leg immediately before the
139 ACB leg; that level would then be compared to the adjacent MinAlt level that begins at the end of the slant descent.
140 Otherwise, MinAlt-BCB pairs that are used include when a MinAlt level leg was immediately preceded or succeeded by a
141 BCB level leg.

142

143 2.2 Implementation of Flight Legs

144 Across ACTIVATE's six deployments, MinAlt and BCB legs were identified for RFs when the Falcon flew cloud
145 ensembles (Fig. 1). There were several instances when the MinAlt and BCB legs were not immediately adjacent and
146 separated by another leg, such as at ACB (i.e., the flight order was BCB-ACB-MinAlt; Fig. 1). In those cases, to get
147 MinAlt/BCB pairs that were closer in time, our method involved identifying the BCB altitude during the slant
148 altitudinal change (either descent or ascent) between MinAlt-ACB based on the altitude of the BCB leg immediately
149 before the ACB leg (see red star in Fig. 1). A secondary check was made to ensure that identified BCB leg was below
150 cloud base using 1-Hz LWC and N_d values from the FCDP (criteria in Sect. 2.5). The vertical structure of the layer
151 between MinAlt and BCB was examined using data between the last time stamp in the MinAlt/BCB leg (i.e.,
152 whichever was first in the MinAlt-BCB pair) and first-time stamp in the subsequent BCB/MinAlt leg (i.e., whichever
153 was second in the MinAlt-BCB pair). For simplicity, we refer to the case of using BCB data during slant profiles as
154 "legs" too, even though they were not level legs. This study compares various measurement data (Sect. 2.5) between
155 MinAlt and BCB legs using the last/first 5 seconds of data during adjacent MinAlt-BCB legs, and in the case of slants,
156 we use the 2 points before and after the actual BCB point (for a total of 5; average altitude range ~ 20 m) to represent
157 the BCB level with the condition that all data were out of cloud.



158

159 **2.3 Instrumentation**

160 A summary of instrumentation relevant to this study is shown in Table 2 and briefly described here. A nephelometer
 161 (TSI-3563) measured the dry scattering coefficient at 550 nm (particle diameter (D_p) $< 5.0 \mu\text{m}$ for 2020 and $D_p < 1.0$
 162 μm for 2021 and 2022); a Laser Aerosol Spectrometer (LAS; TSI-3340) measured aerosol size distributions ($0.1 \mu\text{m}$
 163 $< D_p < 5.0 \mu\text{m}$) and here we use the integrated aerosol volume concentration data; a Fast Cloud Droplet Probe (FCDP;
 164 SPEC Inc.) measured liquid water content (LWC) and particle and cloud drop size distributions between 3 and 50 μm ;
 165 a two-dimensional stereo (2D-S; SPEC Inc.; $25 \mu\text{m} < D_p < 1500 \mu\text{m}$) probe provided LWC, liquid droplet effective
 166 diameter, and an ice flag, where the ice flag is equal to 1 if ice was detected (otherwise the variable is equal to 0); a
 167 diode laser hygrometer (DLH) measured the water vapor mixing ratio (q_v); a turbulent air motion measurement system
 168 (TAMMS) measured three-dimensional winds (Thornhill et al., 2003); and an axial cyclone cloud water collector
 169 (AC3) (Crosbie et al., 2018) collected cloud water samples by inertially separating droplets from the air stream.
 170 Collected cloud water samples were then analyzed post-flight with ion chromatography (IC) with operating conditions
 171 summarized elsewhere (Corral et al., 2022; Gonzalez et al., 2022). Section 2.6 describes the cloud water data in more
 172 detail.

173

174 **Table 2: Summary of field campaign instrumentation used and corresponding measurements.**

175

Instruments	Measurements	Diameter (μm)	Reference
TSI-3563 Nephelometer	Dry scattering coefficient at 550 nm	< 5.0 for 2020; < 1.0 for 2021 & 2022	Ziemba et al. (2013)
TSI-3340 Laser Aerosol Spectrometer (LAS)	Integrated aerosol volume concentration	0.1 – 5.0	Froyd et al. (2019)
SPEC Inc. Fast Cloud Droplet Probe (FCDP)	Liquid water content (LWC), particle number concentration (N_a), cloud drop number concentration (N_d)	3 – 50	Kirschler et al. (2022)
SPEC Inc. Two-Dimensional Stereo Probe, Horizontal Arm (2DS-H)	LWC, effective diameter for liquid, ice flag	25 – 1500	Kirschler et al. (2023)
Diode Laser Hygrometer (DLH)	Water vapor mixing ratio (q_v)	N/A	Diskin et al. (2002)
Axial Cloud Water Collector (AC3)	Cloud water composition	see Sect. 2.6	Crosbie et al. (2018)
Turbulent Air Motion Measurement System (TAMMS)	Three dimensional winds	N/A	Thornhill et al. (2003)

176



177 2.4 Marine Boundary Layer Coupling

178 2.4.1 Thermodynamic Variables

179 To estimate the degree of coupling within the marine boundary layer, we consider the change in vertical profile of two
180 parameters: total water mixing ratio (q_t) and liquid water potential temperature (θ_ℓ). Relevant to this study are these
181 equations,

$$182 \quad 183 \quad q_\ell = \frac{LWC}{\rho_d} \quad (1)$$

$$184 \quad 185 \quad q_t = q_v + q_\ell \quad (2)$$

186 where the total water mixing ratio is the sum of water vapor mixing ratio (q_v) and liquid water mixing ratio (q_ℓ). The
187 water vapor mixing ratio (q_v) provided by the DLH is converted from ppmv to g kg^{-1} . The liquid water mixing ratio
188 (q_ℓ) is defined as the ratio of the mass of liquid water to the mass of dry air within a unit volume of air, which is
189 equivalent to the ratio of LWC (provided by the FCDP) and the density of dry air (ρ_d).
190

191 Also relevant are these equations,

$$192 \quad 193 \quad \theta = (T + 273.15) \times \left(\frac{p_0}{p}\right)^\kappa \quad (3)$$

$$194 \quad 195 \quad \theta_\ell = \theta - \left(\frac{L_v}{c_{pd}}\right) \times q_\ell \quad (4)$$

196 where in equation 3, T and p are the given temperature in $^\circ\text{C}$ and pressure in hPa from Falcon measurements,
197 respectively, p_0 is the reference pressure (= 1000 hPa), and κ is the ratio of gas constant of dry air (R_d) to the
198 specific heat of dry air at constant pressure (c_{pd}). In equation 4, L_v is latent heat of vaporization and c_{pd} is the specific
199 heat of dry air at constant pressure. When LWC is equal to 0, θ_ℓ is equal to θ . θ_ℓ is useful for the purposes of this study
200 as it is not significantly influenced by evaporating precipitation. Information regarding LWC thresholds for MinAlt-
201 BCB pairs is included in Sect. 2.5.
202

203

204 For each MinAlt and BCB leg, the average θ_ℓ and q_t across the leg was calculated and the difference between the two
205 layers was taken as follows:

206

$$207 \quad \Delta q_t = q_{t,MinAlt} - q_{t,BCB^*} \quad (5)$$

208

$$209 \quad \Delta \theta_\ell = \theta_{\ell,BCB^*} - \theta_{\ell,MinAlt} \quad (6)$$

210

211 where in both equations 5-6, the order of legs on the right-hand side is meant to arrive at a positive value for the
212 difference based on expectation.

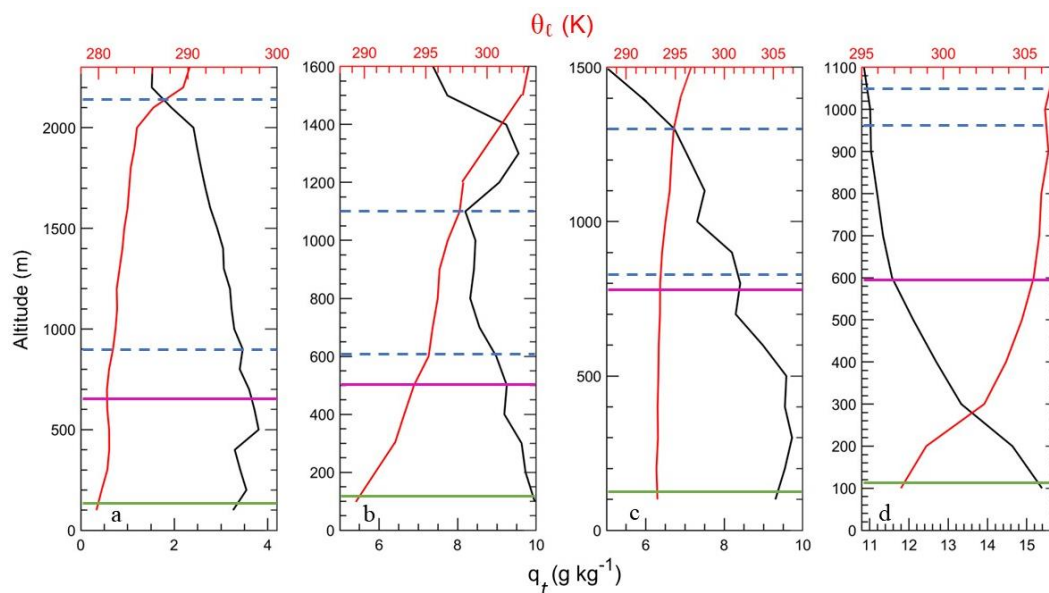


213

214 **2.4.2 Coupling Criteria**

215 The criteria we use for the different coupling regimes were informed by (but are not identical to) those used in past
 216 work (Jones et al., 2011; Dong et al., 2015; Wang et al., 2016; Su et al., 2022). Our focus was on comparing the vertical
 217 range between MinAlt and BCB legs due to the focus on examining aerosol characteristics in particular within that
 218 range and also cloud microphysical conditions above cloud base. To qualify as strongly coupled, the difference
 219 between MinAlt and BCB had to satisfy these conditions: $\Delta q_t \leq 0.8 \text{ g kg}^{-1}$ and $\Delta \theta_t \leq 1.0 \text{ K}$ (example in Fig. 2a). Since
 220 Δq_t is more influenced by evaporation and condensation whereas $\Delta \theta_t$ is more affected by air mass mixing (such as
 221 entrainment) and diabatic heating and cooling, it is proposed to have two degrees of moderate coupling – when one
 222 of Δq_t and $\Delta \theta_t$ fit the strong coupling criteria and the other did not (Fig. 2b-c). Finally, profiles are considered “weakly
 223 coupled” when both Δq_t and $\Delta \theta_t$ do not satisfy the strong coupling criteria values (Fig. 2d). Vertical profiles of q_t and
 224 θ_t were examined for all MinAlt/BCB pairs to ensure robustness of the categorization method. The use of the two
 225 moderate categories is exploratory in nature and meant to identify if differences are found between both themselves
 226 and the more extreme categories of strong and weak. Appendix A further explores differences between the two
 227 moderate regimes and suggests that the moderately coupled category with high $\Delta \theta_t$ is influenced more by processes
 228 above the MBL such as entrainment of dry air with high potential temperature whereas the other moderate category
 229 with high Δq_t is influenced by surface processes.

230



231

232 **Figure 2: Representative vertical profiles of θ_t and q_t for (a) strong coupling from RF 44 on 3 February 2021, (b) moderate**
 233 **coupling with high $\Delta \theta_t$ from RF 150 on 5 May 2022, (c) moderate coupling with high Δq_t from RF 66 on 5 May 2021, and**
 234 **(d) weak coupling from RF 158 on 20 May 2022. The dashed blue lines demarcate the cloud top and base levels, the magenta**



235 **line indicates the BCB leg, and the green line indicates the MinAlt leg. There was a total of 411 MinAlt-BCB pairs analyzed**
236 **in this study.**

237

238 **2.5 Aerosols and Atmospheric Properties**

239 There were several aerosol and atmospheric properties investigated in this study: aerosol scattering (scat) at 550 nm
240 ($< 5 \mu\text{m}$ in 2020 and $< 1 \mu\text{m}$ in 2021-2022), integrated volume (IntV: $0.1 < D_p < 5 \mu\text{m}$), particle number concentration
241 (N_a ; $3 < D_p < 50 \mu\text{m}$), cloud drop number concentration (N_d ; $3 < D_p < 50 \mu\text{m}$), and turbulence (σ_w). Note that the N_a
242 measurement from the FCDP for diameter $> 3 \mu\text{m}$ is important in this study to better isolate sea salt particles (Gonzalez
243 et al., 2022). The integrated volume also is expected to be influenced by larger sea salt particles in the measurement
244 size range. These properties were averaged across each MinAlt and BCB pair and the difference between the MinAlt
245 and BCB values was computed. To account for interference from cloud droplet shatter with the aerosol statistics, we
246 only looked at MinAlt-BCB pairs when atmospheric conditions for each leg was devoid of cloud, rain, and ice. The
247 following three criteria had to be met: (1) ice flag from 2DS-H = 0, (2) effective liquid diameter from 2DS-H $< 60 \mu\text{m}$,
248 and (3) LWC from FCDP $< 0.005 \text{ g m}^{-3}$, to filter out conditions with ice, liquid precipitation, and clouds, respectively.
249 When considering in-cloud conditions for N_d , additional criteria were needed based on FCDP data: LWC $> 0.05 \text{ g m}^{-3}$
250 and $N_d > 10 \text{ cm}^{-3}$ (Kirschler et al., 2023). N_d data was collected from ACB legs closest in proximity to a MinAlt-
251 BCB pair ($< 30 \text{ min}$; 60% within 10 min) due to one of the study objectives being to examine how N_d varies between
252 the four defined coupling regimes. Turbulence was calculated as the standard deviation of the vertical wind velocity
253 for a level leg as done in other work (e.g., MacDonald et al., 2020).

254

255 **2.6 Cloud Water Species**

256 The nine cloud water species of interest in this study include non-sea salt calcium (nss- Ca^{2+}), chloride (Cl^-), potassium
257 (K^+), magnesium (Mg^{2+}), sodium (Na^+), ammonium (NH_4^+), nitrate (NO_3^-), oxalate, and non-sea salt sulfate (nss-
258 SO_4^{2-}). Calculations of nss- Ca^{2+} and nss- SO_4^{2-} utilized mass ratios and concentrations of pure Ca^{2+} , Na^+ , and SO_4^{2-} ,
259 following the methodology outlined in Sect. 2.7 of AzadiAghdam et al. (2019). The IC is used to obtain concentrations
260 of cloud water species in aqueous units (mg L^{-1}), which were then converted to air equivalent concentrations using the
261 methods described in Gonzalez et al. (2022). Briefly, the cloud water sample was considered in-cloud under the criteria
262 $\text{LWC}_{\text{FCDP}} > 0.05 \text{ g m}^{-3}$. When this condition was met, the concentration was multiplied by the average LWC_{FCDP}
263 measured across the sampling time and divided by the density of water and ultimately converted to $\mu\text{g m}^{-3}$ for the air
264 equivalent concentration. These units allow one to compare concentrations more fairly between samples to remove
265 biases due to varying amounts of water in different clouds. As cloud water samples were collected periodically during
266 flights, samples were only examined when a MinAlt or BCB leg being investigated was within 30 minutes or
267 overlapped with the collection period. Out of a total of 535 cloud water samples over the 6 deployments, 67 met the
268 criteria to be used for this study's MinAlt/BCB pairs. Statistics including mean, standard deviation (std. dev.),
269 minimum, maximum, and quartile ranges were calculated across the 67 data points for all nine cloud water species.

270

271 Additionally, cumulative average cloud water mass concentrations and mass fractions were calculated for the 67
272 samples. The total mass concentration for each coupling regime was found by the summation of only the nine chemical



273 species investigated in this manuscript. Welch's t-test calculations were conducted to compare the mean concentrations
274 of the investigated chemical species across coupling regimes. These tests were done in lieu of the traditional t-test due
275 to the assumption that the data used have unequal variances and thus are slightly more robust.

276

277 3 Results and Discussion

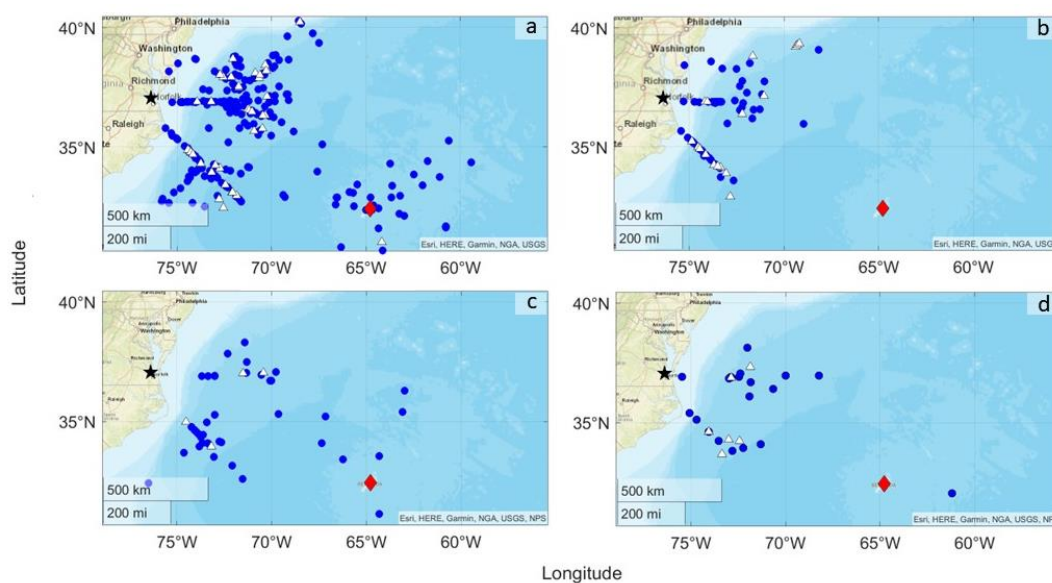
278 3.1 Thermodynamic Criteria

279 This section discusses the application of the developed thermodynamic criteria across all MinAlt-BCB pairs. In total,
280 411 MinAlt-BCB pairs were investigated (pair locations shown in Fig. 3), with the breakdown of the distribution
281 across the different degrees of coupling shown in Fig. 4 and Table 3. The majority of the pairs were classified as
282 strongly coupled, with a breakdown of 71.29% (strongly coupled), 13.63% (moderately coupled with high $\Delta\theta_t$),
283 10.22% (moderately coupled with high Δq_t), and 4.86% (weakly coupled). Strong turbulent mixing in the northwest
284 Atlantic Ocean, especially during the winter (Brunke et al., 2022) which is when most pairs were identified, is likely
285 why the majority of pairs were found to be strongly coupled, as the coupling parameters θ_t and q_t are relatively constant
286 vertically from the surface to near cloud bases due to the strong mixing (Fig. 2a).

287

288 There are no major spatial distribution differences for MinAlt-BCB pairs across the four coupling regimes with minor
289 exceptions being that the majority of pairs identified farther offshore around Bermuda were for both the strongly
290 coupled and moderately coupled with high Δq_t categories. Also, the strong and moderate coupling with high $\Delta\theta_t$
291 categories had more pairs north of 37.5°N, which coincides with more wintertime sampling of cold air outbreak events
292 that feature turbulent conditions (e.g., Painemal et al., 2021; Kirschler et al., 2022).

293



294



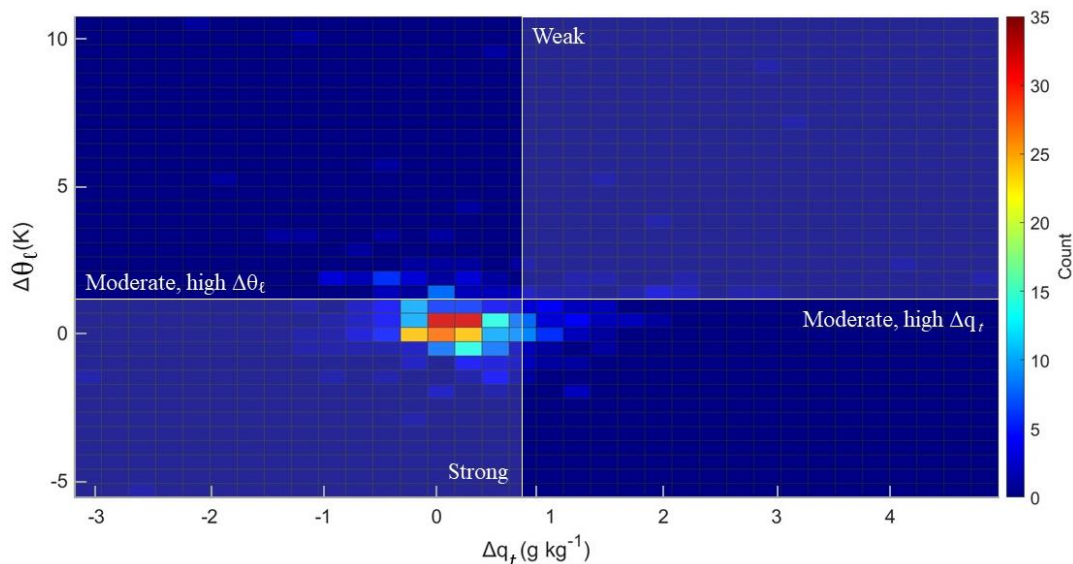
295 **Figure 3: Locations of the BCB segments of the MinAlt-BCB pairs (blue circles), broken up into the four different degrees**
 296 **of coupling: (a) strong, (b) moderate, high $\Delta\theta_t$, (c) moderate, high Δq_t , and (d) weak. The MinAlt legs were close in time to**
 297 **the BCB legs, so only one spatial map is needed to show the approximate data point location for each pair. The locations of**
 298 **the cloud water samples (white triangles) are overlaid on the BCB segment locations. The black star indicates the location**
 299 **of NASA Langley Research Center, and the red diamond indicates Bermuda.**

300

301 **Table 3: Total count of MinAlt-BCB pairs categorized into four coupling categories. The winter months include January,**
 302 **February, March, and April, while the summer months include May, June, August, and September.**

	Strong coupling	Moderate coupling, high $\Delta\theta_t$	Moderate coupling, high Δq_t	Weak coupling
All	293	56	42	20
Summer	118	12	18	11
Winter	175	44	24	9

303



304

305 **Figure 4: Joint frequency histogram of $\Delta\theta_t$ versus Δq_t for MinAlt-BCB pairs, categorized into four coupling regimes. There**
 306 **is a total of 411 pairs plotted (strong coupling = 293, moderate coupling with high $\Delta\theta_t$ = 56, moderate coupling with high**
 307 **Δq_t = 42, weak coupling = 20). Figure S1 is a similar scatterplot that breaks down the MinAlt-BCB pairs into seasons.**

308

309 Figure S1 shows the seasonal distribution of the MinAlt-BCB pairs from summer and winter deployments (counts
 310 provided in Table 3). There were more MinAlt-BCB pairs during the winter versus summer (252 vs. 159) largely due
 311 to the greater ease of sampling such cases with the higher wintertime cloud fraction in the region (Painemal et al.,
 312 2021; Kirschler et al., 2022, 2023). But generally, the distribution of coupling categories was the same
 313 (summer/winter): 74.21/69.44% strongly coupled, 7.55/17.47% moderately coupled with high $\Delta\theta_t$, 11.32/9.52%



314 moderately coupled with high Δq , and 6.92/3.57% weakly coupled. The frequency of the moderately coupled with
 315 high Δq category was relatively higher in summer versus winter compared to the other moderate category, which is
 316 coincident with the summer having higher temperatures (i.e., higher q_v) and more flights farther south in Fig. 3 where
 317 temperatures are warmer as compared to farther north.

318

319 For context, applying the criteria from past work in Table 1 (Jones et al., 2011; Dong et al., 2015) to this dataset (i.e.,
 320 Δq_t [g kg^{-1}] and $\Delta \theta_\ell$ [K]) < 0.5 for coupled and all others decoupled) would have led to 206 and 205 coupled and
 321 decoupled cases, respectively, with a seasonal breakdown as follows (summer/winter): 42.72/57.28% coupled,
 322 34.63/65.37% decoupled. However, we caution that the compared vertical levels differ between these studies. For
 323 example, Jones et al. (2011) compared levels encompassing more of the full extent of the cloudy MBL (e.g., somewhat
 324 analogous to the use of MinAlt and BCT in Fig. 1), whereas in this study we compare MinAlt to BCB due to our focus
 325 on aerosol characteristics, which are difficult to measure in clouds. Also, the frequency of occurrence of the four
 326 coupling regimes in this study are driven in part by how flights were designed to fly towards areas with relatively
 327 higher cloud fraction without complicating scenes such as with multiple cloud layers; thus, the results in Table 3 and
 328 Figure 4 for instance are not a fully accurate depiction of the actual frequency of occurrence over the northwest Atlantic
 329 but rather more of a summary of what was experienced during ACTIVATE flights.

330

331 3.2 Aerosol and Atmospheric Properties

332 The results of the aerosol and atmospheric parameter calculations across the four different coupling regimes are
 333 provided in Table 4 (seasonal results in Tables S1-S2). Of the 411 MinAlt-BCB pairs, 293 were used in aerosol
 334 calculations after eliminating pairs that may have been influenced by rain, cloud, or ice interference. As a note, when
 335 quantifying altitudinal differences in variables across different coupling regimes, the mean at each altitude is used as
 336 the comparison parameter unless otherwise stated, as outliers were already removed prior to data analysis.

337

338 The first hypothesis of this study is that strongly coupled regimes would have greater turbulence (σ_w) than weakly
 339 coupled regimes. This hypothesis is confirmed when examining σ_w results at both MinAlt (strong/weak = 0.86/0.55
 340 m s^{-1}) and BCB levels (strong/weak = 0.70/0.49 m s^{-1}). The two categories of moderate coupling had greater turbulence
 341 at both altitudes compared to weak coupling, and sometimes had greater turbulence than pairs categorized as strongly
 342 coupled. This suggests considering multiple coupling regimes for the northwest Atlantic is important to tease out such
 343 nuances as differences in the thermodynamic profiles can potentially coincide with different aerosol and cloud
 344 characteristics as discussed subsequently.

345

346 **Table 4: Statistics for various atmospheric properties investigated across the MinAlt-BCB pairs (Δ calculation refers to the**
 347 **MinAlt value minus the BCB value), except for MinAlt σ_w and BCB σ_w , which are the average σ_w for each respective leg**
 348 **and for N_a , which is calculated in ACB legs. Each property is broken down into the different degrees of coupling (n = number**
 349 **of points used in each coupling category). Variable acronyms defined in Sect. 2.5.**

Degree of Coupling	Mean	Std. Dev.	Min	25%	50%	75%	Max	n
--------------------	------	-----------	-----	-----	-----	-----	-----	---



Δscat	Strong	2.2	2.1	0.00	0.78	1.7	2.8	13.9	274
	Moderate, high $\Delta\theta_\ell$	3.5	3.5	0.07	0.97	2.4	4.6	14.6	52
	Moderate, high Δq_r	2.4	2.1	0.01	0.70	1.8	3.6	9.2	39
	Weak	3.5	3.3	0.01	0.88	2.2	6.6	10.8	20
ΔIntV	Strong	2.5	2.6	0.02	0.67	1.7	3.5	13.6	288
	Moderate, high $\Delta\theta_\ell$	2.1	2.2	0.00	0.46	1.5	2.9	9.3	54
	Moderate, high Δq_r	1.9	1.9	0.01	0.46	1.2	2.8	8.3	41
	Weak	2.8	2.3	0.18	1.0	2.4	4.2	7.6	20
$\Delta N_{a>3\mu\text{m}}$	Strong	0.32	0.55	0.00	0.05	0.13	0.35	4.9	288
	Moderate, high $\Delta\theta_\ell$	0.33	0.64	0.00	0.03	0.13	0.31	3.6	54
	Moderate, high Δq_r	0.15	0.14	0.00	0.06	0.11	0.21	0.61	41
	Weak	0.53	1.5	0.01	0.02	0.08	0.27	5.9	20
N_d	Strong	344	217	19	193	310	473	954	238
	Moderate, high $\Delta\theta_\ell$	419	242	45	228	374	610	962	48
	Moderate, high Δq_r	329	154	25	235	327	430	671	31
	Weak	275	181	50	107	245	411	606	18
MinAlt σ_w	Strong	0.86	0.49	0.00	0.47	0.79	1.2	2.4	293
	Moderate, high $\Delta\theta_\ell$	1.0	0.57	0.00	0.52	1.1	1.3	2.2	56
	Moderate, high Δq_r	0.81	0.44	0.00	0.51	0.73	0.99	1.9	42
	Weak	0.55	0.38	0.00	0.19	0.51	0.90	1.3	20
BCB σ_w	Strong	0.70	0.62	0.00	0.26	0.60	1.0	4.0	293
	Moderate, high $\Delta\theta_\ell$	0.64	0.62	0.00	0.00	0.53	1.1	2.2	56
	Moderate, high Δq_r	0.81	0.76	0.00	0.26	0.71	1.1	3.3	42
	Weak	0.49	0.50	0.00	0.04	0.30	0.87	1.6	20
BCB - MinAlt σ_w	Strong	-0.15	0.66	-2.0	-0.45	-0.16	0.10	3.6	285
	Moderate, high $\Delta\theta_\ell$	-0.34	0.57	-2.2	-0.81	-0.23	0.10	0.59	53
	Moderate, high Δq_r	0.01	0.74	-1.6	-0.28	-0.08	0.20	2.9	42
	Weak	-0.05	0.47	-1.1	-0.35	0.01	0.25	0.90	20

350

351 The second hypothesis is that aerosol scattering (Δscat), integrated volume ($0.1 < D_p < 5 \mu\text{m}$; ΔIntV), and giant particle
 352 number concentration ($3 < D_p < 50 \mu\text{m}$; $\Delta N_{>3\mu\text{m}}$) would have more homogenous concentrations (i.e., smaller MinAlt-
 353 BCB differences) in strongly coupled regimes compared to weakly coupled regimes due to greater mixing for the
 354 former as supported by the higher σ_w results already shown. This hypothesis is supported (Table 4) since strong
 355 coupling cases exhibited lower mean differences (MinAlt-BCB) than weak coupling (Δscat : $2.2/3.5 \text{ Mm}^{-1}$, ΔIntV :
 356 $2.5/2.8 \mu\text{m}^3 \text{ cm}^{-3}$, and $\Delta N_{>3\mu\text{m}}$: $0.3/0.5 \text{ cm}^{-3}$, for strong/weak regimes). The third hypothesis was that cloud drop number
 357 concentration ($3 < D_p < 50 \mu\text{m}$; N_d) would be greater in strong coupling conditions, as stronger updrafts and turbulence
 358 would help to activate more particles into cloud droplets (this was also found in Dong et al., 2015). This is confirmed
 359 in Table 4: mean N_d : $344/275 \text{ cm}^{-3}$ for strong/weak regimes for ACB legs coinciding with each MinAlt-BCB pair. This
 360 result is consistent with past studies for the northwest Atlantic linking stronger turbulence to greater droplet activation
 361 efficiency (Kirschler et al., 2022; Dadashazar et al., 2021). The results based on medians agree with those of mean
 362 values in Table 4.

363

364 When comparing the moderate coupling regimes with the strong and weak regimes, neither Δscat , ΔIntV , nor $\Delta N_{>3\mu\text{m}}$
 365 showed a consistent trend in terms of being higher or lower across all three variables. However, one consistent feature
 366 among the moderate regimes is that the moderate high Δq_r category showed smaller differences than moderate high



367 $\Delta\theta_t$ for the three aerosol variables. Sometimes, the difference calculations with the lowest values did not occur during
 368 the strong coupling cases, but rather during moderate coupling with high Δq_t cases (i.e., $\Delta\text{IntV} = 1.9 \mu\text{m}^3 \text{cm}^{-3}$, $\Delta N_{>3\mu\text{m}}$
 369 $= 0.2 \text{cm}^{-3}$). These low differences presumably should coincide with the highest values of σ_w . This is somewhat
 370 supported by how BCB σ_w was greatest for the moderate coupling with high Δq_t regime ($0.81 \pm 0.76 \text{m s}^{-1}$), although
 371 MinAlt σ_w was greatest for the moderate coupling with high $\Delta\theta_t$ regime ($1.00 \pm 0.57 \text{m s}^{-1}$) with the value for the
 372 moderate coupling with high Δq_t regime being $0.81 \pm 0.44 \text{m s}^{-1}$. Also, Appendix A provides discussion in support of
 373 why the high Δq_t category may have small aerosol differences between MinAlt and BCB levels, whereby surface
 374 effects may be at play to help promote mixing in the MBL. Interestingly, the highest N_d values were for the moderate
 375 high $\Delta\theta_t$ category with a mean of 419cm^{-3} , which can partly be explained by how most of these cases occurred during
 376 the winter flights when N_d is higher than in the summer (see also Tables S1 and S2) due to strong updraft velocities
 377 that efficiently activate particles into droplets (e.g., Kirschler et al., 2022). These conditions in winter were common
 378 during cold air outbreaks (Dadashazar et al., 2021).

379

380 3.3 Cloud Water Species

381 67 cloud water samples were used in this study (Table 5), with 59.70% of the samples falling into the strong coupling
 382 regime, followed by moderate coupling with high $\Delta\theta_t$ (25.37%), weak coupling (8.96%), and lastly moderate coupling
 383 with high Δq_t (5.97%). Locations of samples are shown in Fig. 3. Within the strong coupling and moderate coupling
 384 with high $\Delta\theta_t$ categories, there were several samples north of 37°N , whereas the moderate coupling with high Δq_t and
 385 weak coupling samples were all south of that latitude. The former two categories include substantially more data
 386 during the winter when air masses typically come from the continent featuring urban emissions (Dadashazar et al.,
 387 2022a).

388

389 **Table 5: Average cloud water mass concentrations ($\mu\text{g m}^{-3}$) and mass fractions (in %) for all cloud water samples. Also**
 390 **shown is the pH and Cl⁻:Na⁺ mass ratio. Results are categorized into different degrees of coupling, and the ratio of weak-**
 391 **to-strong coupling is also reported.**

392

	Strong	Moderate, high $\Delta\theta_t$	Moderate, high Δq_t	Weak	Weak : Strong
Mass concentration ($\mu\text{g m}^{-3}$)					
Total	87.45	57.93	91.92	10.32	0.12
Cl ⁻	45.6	32.0	52.2	4.1	0.09
Na ⁺	27.9	18.6	29.9	2.5	0.09
Mg ²⁺	3.33	2.22	3.59	0.35	0.10
K ⁺	0.56	0.37	0.59	0.05	0.09
nss-Ca ²⁺	0.53	0.18	0.17	0.03	0.06
nss-SO ₄ ²⁻	2.6	1.5	1.7	1.2	0.47
NO ₃ ⁻	6.0	2.7	3.3	1.5	0.26



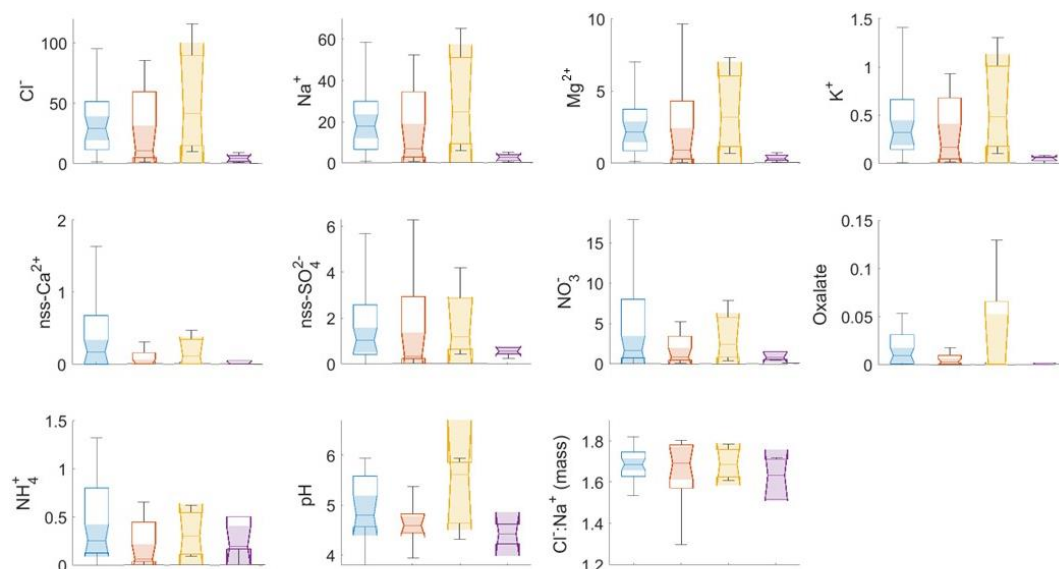
Oxalate	0.10	0.01	0.03	0.01	0.14
NH ₄ ⁺	0.89	0.37	0.33	0.56	0.63
Mass fraction (%)					
Cl ⁻	52.11	55.21	56.79	39.48	0.76
Na ⁺	31.94	32.07	32.56	24.31	0.76
Mg ²⁺	3.81	3.84	3.91	3.38	0.89
K ⁺	0.64	0.63	0.65	0.48	0.75
nss-Ca ²⁺	0.60	0.32	0.19	0.31	0.51
nss-SO ₄ ²⁻	2.93	2.65	1.90	11.56	3.95
NO ₃ ⁻	6.86	4.63	3.63	14.95	2.18
Oxalate	0.11	0.01	0.04	0.13	1.20
NH ₄ ⁺	1.02	0.63	0.35	5.41	5.32
Cl ⁻ :Na ⁺ mass ratio and pH					
pH	4.92	4.60	5.29	4.44	0.90
Cl ⁻ :Na ⁺	1.65	1.66	1.69	1.53	0.92
n	40	17	4	6	

393

394 Figure 5 provides composition statistics for the cloud water samples categorized into the four coupling regimes. As a
 395 note, the notches (and shading) of the box plots help to compare air-equivalent mass concentration medians across the
 396 different coupling categories and aid in the determination of statistical significance. Since this study has utilized means
 397 instead of medians when comparing values across coupling regimes, mean concentrations are provided in the SI
 398 (Tables S3-S5) and the results of Welch's t-tests for each category are given in Table S6. This study also investigated
 399 cumulative average mass concentrations and mass fractions (Table 5) to paint a clearer picture of the breakdown of
 400 chemical species for different degrees of coupling. Based on previous work for stratocumulus clouds over the northeast
 401 Pacific (Wang et al., 2016), we hypothesize that samples from strong coupling regimes would have higher mass
 402 concentrations compared to weakly coupled regimes owing to higher concentrations of sea salt constituents (e.g., Cl⁻
 403 , Na⁺, Mg²⁺, and K⁺). More turbulent conditions in strongly coupled cases are thought to promote more mixing of sea
 404 salt into boundary layer clouds, which can be detected with cloud water composition measurements (e.g., Dadashazar
 405 et al., 2017).

406

407



408

409 **Figure 5: Notched box plots of species concentrations ($\mu\text{g m}^{-3}$), $\text{Cl}^-:\text{Na}^+$ mass ratio, and pH from cloud water samples**
410 **collected during periods coinciding with MinAlt-BCB pairs. The box plots are colored according to degree of coupling: blue**
411 **(strong), red (moderate, high $\Delta\theta_i$), yellow (moderate, high Δq_i), and purple (weak). The notches of the boxes assist in the**
412 **determination of statistical significance between multiple medians (the shading indicates where the notches begin and end).**
413 **If notches/shading do not overlap, the medians are statistically different from one another (also referred to as statistically**
414 **significant). Table S6 provides the results of Welch's t-tests, which compares the means of two groups and determines if**
415 **they are statistically different. The tests were performed on the mean cloud water concentrations of these nine chemical**
416 **species, pH, and $\text{Cl}^-:\text{Na}^+$.**

417

418 Strong coupling regime samples exhibit higher average mass concentrations compared to weak coupling, and Na^+ , Cl^-
419 , K^+ , and NO_3^- were all found to be statistically different across the two regimes (p-values: 1.07E^{-4} , 3.54E^{-5} , 5.52E^{-5} ,
420 and 9.57E^{-3} , respectively). The most abundant species by mass across the coupling regimes were usually Cl^- , Na^+ , and
421 NO_3^- , similar to the results of Wang et al. (2016). Further, although lower in absolute mass concentration, some species
422 were relatively more abundant (i.e., higher mass fraction) in the weak coupling regime: nss- SO_4^{2-} (11.56% [weak] vs.
423 2.93% [strong]), NO_3^- (14.95% [weak] vs. 6.86% [strong]), NH_4^+ (5.41% [weak] vs. 1.02% [strong]). Oxalate was
424 very low in overall concentration and exhibited comparable mass fractions: 0.13% [weak] vs. 0.11% [strong]. These
425 results are consistent with the idea of surface emissions (mainly sea salt) driving cloud water composition in turbulent
426 conditions (i.e., strongly coupled) in contrast to weakly coupled clouds that have much lower overall mass
427 concentrations of the reported ions but relatively more influence from non-sea salt species. The two moderate coupling
428 regimes include samples with concentration and mass fraction values more similar to the strongly coupled regime,
429 with even higher sea salt tracer species concentrations for the moderate high Δq_i regime. This is consistent with the
430 aerosol results in Sect. 3.2 that suggested this latter category can have appreciable influence from the surface.

431



432 Wang et al. (2016) analyzed 35 cloud water constituents for northeast Pacific stratocumulus clouds and found that 27
433 chemical species were higher in coupled clouds, with the remaining eight (acetate, formate, Si, NO_2^- , Al, Mn, Cr, and
434 Co) higher in decoupled clouds due to relatively more continental influence. The 27 cloud water species that were
435 higher in coupled clouds were associated with a mix of anthropogenic and natural sources (i.e., sea salt emissions for
436 Cl^- and Na^+). Conversely, the eight species that were higher in decoupled clouds were associated with crustal matter
437 and biogenic sources. Several of the most abundant species from our study (Na^+ , Cl^- , Mg^{2+}) are common sea salt
438 tracers, while NO_3^- sources in the region may include ocean sea spray and biogenic emissions, wildfires, agricultural
439 emissions, and ship exhaust (Corral et al., 2020; Corral et al., 2021; Corral et al., 2022; Shah et al., 2018). Note that
440 nitric acid can partition effectively into cloud droplets as well, which can drive up cloud water NO_3^- levels (e.g.,
441 Prabhakar et al., 2014). At least some of the species with higher mass fractions in the weakly coupled regime (e.g.,
442 nss-SO_4^{2-} , NO_3^-) have previously been linked to combustion sources in this region, such as industrial emissions and
443 transportation (Brock et al., 2008; Song et al., 2001). Ammonium is a major base forming salts with nss-SO_4^{2-} and
444 NO_3^- , whereas oxalate has diverse sources (e.g., continental, marine) and can be associated with sea salt and produced
445 via cloud processing (e.g., Stahl et al., 2020; Hilario et al., 2021). Nss-Ca^{2+} is often associated with continental crustal
446 matter (Ma et al., 2021; Edwards et al., 2024), and its concentrations are generally very low. Similar to oxalate, these
447 suggest a low influence of dust during the majority of ACTIVATE flights.

448

449 In addition to examining mass concentrations, we also examined pH and the $\text{Cl}^-:\text{Na}^+$. Regarding the latter ratio, sea
450 salt chloride concentrations can be reduced in the presence of acidic species such as sulfuric and nitric acids (e.g.,
451 Braun et al., 2017; Edwards et al., 2024). This phenomenon is known as Cl^- depletion, and it can be calculated by
452 taking the ratio of $\text{Cl}^-:\text{Na}^+$. For context, Wang et al. (2016) reported no major difference in the $\text{Cl}^-:\text{Na}^+$ ratio in cloud
453 water over the northeast Pacific but measured lower pH in coupled clouds (4.26) versus decoupled clouds (4.48). In
454 this study, samples in the weak coupling regime exhibited the lowest pH (4.4 vs. 5.0 for strong coupling) and $\text{Cl}^-:\text{Na}^+$
455 (1.5 vs. 1.7 for strong coupling), which potentially could be related to the higher relative amount of nss-SO_4^{2-} , NO_3^- .
456 The two moderate coupling regimes feature samples with pH and $\text{Cl}^-:\text{Na}^+$ values more similar to strongly coupled
457 samples.

458

459 A limitation in this analysis is that there were only six cloud water samples that fell into the weak coupling regime.
460 Future work examining the sensitivity of aerosol and cloud characteristics to coupling regimes should try to obtain
461 better sampling coverage across all regimes.

462

463 **4 Conclusions**

464 This study used data collected during the NASA ACTIVATE mission (2020–2022) from the HU-25 Falcon to assess
465 the frequency of different degrees of MBL cloud coupling and also how aerosol and cloud characteristics varied among
466 four such regimes. MinAlt and BCB legs were used to assess thermodynamic statistics along with turbulence, aerosol,
467 and cloud variables, which were calculated at each leg and the differences of the two legs were taken for final



468 comparison metrics. Cloud water species and N_d values associated with MinAlt and BCB pairs were analyzed when
469 cloud sampling occurred within 30 minutes of a MinAlt-BCB pair.

470

471 Vertical profiles between MinAlt and BCB pairs were divided into four degrees of coupling: strongly coupled ($\Delta q_t \leq$
472 0.8 g kg^{-1} , $\Delta\theta_t \leq 1.0 \text{ K}$), moderately coupled with high $\Delta\theta_t$ ($\Delta q_t \leq 0.8 \text{ g kg}^{-1}$, $\Delta\theta_t > 1.0 \text{ K}$), moderately coupled with
473 high Δq_t ($\Delta q_t > 0.8 \text{ g kg}^{-1}$, $\Delta\theta_t \leq 1.0 \text{ K}$), and weakly coupled ($\Delta q_t > 0.8 \text{ g kg}^{-1}$, $\Delta\theta_t > 1.0 \text{ K}$). In total, 411 MinAlt-BCB
474 pairs were investigated, along with 67 cloud water samples. Using this coupling categorization criteria, only a handful
475 of weakly coupled MBL clouds were detected (20, compared to 286 with strong coupling). The relative amounts of
476 the regimes did not vary substantially between the winter and summer seasons. Instead, particular focus was placed
477 on comparing regimes with strong coupling to those with weak coupling. Support for the coupling criteria was sought
478 through five different aerosol/cloud/dynamic parameters (Δscat , ΔIntV , $\Delta N_{>3\mu\text{m}}$, N_d , and σ_w) and 11 cloud water
479 variables (nss- Ca^{2+} , Cl^- , K^+ , Mg^{2+} , Na^+ , NH_4^+ , NO_3^- , oxalate, nss- SO_4^{2-} , pH, $\text{Cl}^-:\text{Na}^+$). Turbulence was generally greater
480 during regimes of strong coupling compared to weak coupling, which corresponded to lower values of Δscat , ΔIntV ,
481 and $\Delta N_{>3\mu\text{m}}$ due to better presumed mixing in the MBL. N_d was higher for strong coupling regimes, as higher
482 turbulence likely encouraged more cloud drop activation, which was also observed in Dong et al. (2015) for the
483 northeast Atlantic. Sea salt tracers (e.g., Na^+ , Cl^- , and K^+) were higher in concentration in strongly coupled compared
484 to weakly coupled MBL clouds and were found to have statistically significant differences across the two coupling
485 regimes. Additionally, nss- SO_4^{2-} , NO_3^- , and NH_4^+ which are linked to continental sources, were found in higher mass
486 fractions during weak coupling regimes, which was also observed in Wang et al. (2016) for northeast Pacific
487 stratocumulus clouds, corresponding to lower values of both cloud water pH and the $\text{Cl}^-:\text{Na}^+$ ratio.

488

489 The inclusion of two moderate coupling categories is shown to be insightful as differences between the two potentially
490 can be explained by the relative influence of subsidence/entrainment versus surface effects. More specifically, the
491 moderately coupled category with high $\Delta\theta_t$ is thought to be influenced more by processes above the MBL such as
492 entrainment of dry air with high potential temperature whereas the other moderate category with high Δq_t likely has
493 more influence from surface processes. These speculations are supported by how the moderate high Δq_t regime
494 exhibited even more turbulent mixing than the strong coupling regime, yielding the highest sea salt concentrations in
495 cloud water and the lowest values of ΔIntV and $\Delta N_{>3\mu\text{m}}$. Furthermore, the moderate high $\Delta\theta_t$ category exhibited the
496 highest mean N_d value (419 cm^{-3}) of any category ($275\text{--}344 \text{ cm}^{-3}$ for the other three categories), which can be explained
497 partly by how most of these cases (44 of 56) were in winter flights when N_d is typically higher than summer, especially
498 during cold air outbreaks (e.g., Dadashazar et al., 2021).

499

500 This study is the first to our knowledge to investigate degrees of coupling in MBL clouds through thermodynamic
501 statistics in the northwest Atlantic with a focus on aerosol and cloud microphysical characteristics. Further research
502 of this nature is needed in other regions to assess thermodynamic criteria for MBL cloud to surface coupling, including
503 how aerosol and cloud characteristics change with degrees of MBL coupling in different regions. The results here
504 indicate that a failure to account for different coupling regimes can mix together varying aerosol and cloud



505 microphysical characteristics in data analysis studies, which increases risk of separating out important details such as
506 how cloud composition is very different across the spectrum of cloud coupling strength. A limitation of this study to
507 build on is obtaining more statistics for the more weakly coupled category, which in part may be influenced by how
508 flight plans are designed. The results of this research have important implications for studies of aerosol-cloud
509 interactions, as not considering coupling strength will make interpretations difficult, as we have shown important
510 differences for aerosol and cloud properties.

511

512 **Appendix A. Discussion of the two moderate regimes**

513 To help with the interpretation of the two moderate regimes defined in Table 1, we provide a perspective based on the
514 following discussion. Using equation 1 but expanding it to take the difference of the liquid water potential temperature
515 between the BCB and MinAlt flight legs yields the following:

$$516 \quad \Delta\theta_\ell = (\theta_{BCB} - \left(\frac{L_v}{c_{pd}}\right) \times q_{\ell,BCB}) - (\theta_{MinAlt} - \left(\frac{L_v}{c_{pd}}\right) \times q_{\ell,MinAlt}) \quad (A1)$$

517 Note that both q_ℓ terms are small below cloud. The $\Delta\theta_\ell$ value can thus be large due to large-scale subsidence or
518 entrainment when dry air from free troposphere with high θ which is potentially mixed with air at the BCB level.
519 While θ_{MinAlt} can be high due to surface heating, it acts to reduce $\Delta\theta_\ell$. Also, the current MinAlt is slightly above the
520 typical surface layer and hence the surface inversion. Also, note that:

$$521 \quad \Delta q_t = (q_{v,MinAlt} + q_{l,MinAlt}) - (q_{v,BCB} + q_{l,BCB}) \quad (A2)$$

522 where both q_t terms are small below cloud and are typically much smaller than q_v . The range of q_v is largely controlled
523 by the temperature due to the Clapeyron-Clausius equation (the higher temperature, the higher saturation vapor
524 pressure). While high Δq_t may be due to low q_v at the BCB level, it is more likely due to high q_v near the surface
525 because saturation vapor pressure exponentially increases with temperature.

526 To conclude, the $\Delta\theta_\ell$ term is more likely influenced by features above the MBL while the Δq_t term is more likely
527 influenced by near-surface effects.

528

529 **Data availability**

530 The ACTIVATE dataset can be downloaded at <https://doi.org/10.5067/SUBORBITAL/ACTIVATE/DATA001>
531 (ACTIVATE Science Team, 2020).

532

533 **Author contributions**

534 YC, EC, JPD, GSD, MAF, SK, JBN, MAS, KLT, CV, ELW, and LDZ collected and/or prepared the data. KTZ, SD,
535 and KM conducted data analysis. KTZ, KM, and SD conducted the formal investigation. KTZ, LWS, and AS
536 conducted data interpretation. KTZ and AS prepared the manuscript with editing from all co-authors.

537



538 **Competing interests**

539 At least one of the (co-)authors is a member of the editorial board of Atmospheric Chemistry and Physics.

540

541 **Disclaimer**

542 Publisher's note: Copernicus Publications remains neutral with regard to jurisdictional claims in published maps and
543 institutional affiliations.

544

545 **Acknowledgements**

546 We thank the pilots and aircraft maintenance personnel of NASA Langley Research Services Directorate for
547 conducting ACTIVATE flights and all others who were involved in executing the ACTIVATE campaign.

548

549 **Financial support**

550 ACTIVATE is a NASA Earth Venture Suborbital-3 (EVS-3) investigation funded by NASA's Earth Science Division
551 and managed through the Earth System Science Pathfinder Program Office. University of Arizona investigators were
552 supported by NASA grant no. 80NSSC19K0442 and ONR grant no. N00014-21-1-2115. CV and SK were funded by
553 DFG SPP-1294 HALO under project no. 522359172 and by the European Union's Horizon Europe program through
554 the Single European Sky ATM Research 3 Joint Undertaking projects CONCERTO (grant no 101114785) and
555 CICONIA (grant no 101114613).



556 **References**

- 557 ACTIVATE Science Team: Aerosol Cloud meTeorology Interactions oVer the western ATLantic Experiment Data,
558 <https://doi.org/10.5067/SUBORBITAL/ACTIVATE/DATA001>, 2020.
- 559 Andreae, M. O., Elbert, W., Cai, Y., Andreae, T. W., and Gras, J.: Non-sea-salt sulfate, methanesulfonate, and nitrate
560 aerosol concentrations and size distributions at Cape Grim, Tasmania, *Journal of Geophysical Research:*
561 *Atmospheres*, 104, 21695-21706, <https://doi.org/10.1029/1999JD900283>, 1999.
- 562 Ayers, G. P., Ivey, J. P., and Gillett, R. W.: Coherence between seasonal cycles of dimethyl sulphide,
563 methanesulphonate and sulphate in marine air, *Nature*, 349, 404-406, <https://doi.org/10.1038/349404a0>, 1991.
- 564 AzadiAghdam, M., Braun, R. A., Edwards, E.-L., Bañaga, P. A., Cruz, M. T., Betito, G., Cambaliza, M. O.,
565 Dadashazar, H., Lorenzo, G. R., Ma, L., MacDonald, A. B., Nguyen, P., Simpas, J. B., Stahl, C., and Sorooshian,
566 A.: On the nature of sea-salt aerosol at a coastal megacity: Insights from Manila, Philippines in Southeast Asia,
567 *Atmospheric Environment*, 216, 116922, <https://doi.org/10.1016/j.atmosenv.2019.116922>, 2019.
- 568 Bretherton, C. S. and Wyant, M. C.: Moisture transport, lower-tropospheric stability, and decoupling of cloud-topped
569 boundary layers, *Journal of the Atmospheric Sciences*, 54, 148-167, [https://doi.org/10.1175/1520-0469\(1997\)054<0148:MTLTA>2.0.CO;2](https://doi.org/10.1175/1520-0469(1997)054<0148:MTLTA>2.0.CO;2), 1997.
- 571 Bretherton, C. S., Wood, R., George, R. C., Leon, D., Allen, G., and Zheng, X.: Southeast Pacific stratocumulus clouds,
572 precipitation and boundary layer structure sampled along 20° S during VOCALS-REx, *Atmospheric Chemistry*
573 *and Physics*, 10, 10639-10654, <https://doi.org/10.5194/acp-10-10639-2010>, 2010.
- 574 Brock, C.A., Sullivan, A.P., Peltier, R.E., Weber, R.J., Wollny, A., De Gouw, J.A., Middlebrook, A.M., Atlas, E.L.,
575 Stohl, A., Trainer, M.K. and Cooper, O.R.: Sources of particulate matter in the northeastern United States in
576 summer: 2. Evolution of chemical and microphysical properties, *Journal of Geophysical Research:*
577 *Atmospheres*, 113, D8, <https://doi.org/10.1029/2007JD009241>, 2008.
- 578 Brümmer, B.: Boundary layer mass, water, and heat budgets in wintertime cold-air outbreaks from the Arctic sea ice,
579 *Monthly Weather Review*, 125, 1824-1837, [https://doi.org/10.1175/1520-0493\(1997\)125<1824:BLMWAH>2.0.CO;2](https://doi.org/10.1175/1520-0493(1997)125<1824:BLMWAH>2.0.CO;2), 1997.
- 581 Brunke, M. A., Cutler, L., Urzua, R. D., Corral, A. F., Crosbie, E., Hair, J., Hostetler, C., Kirschler, S., Larson, V., Li,
582 X.-Y., Ma, P.-L., Minke, A., Moore, R., Robinson, C. E., Scarino, A. J., Schlosser, J., Shook, M., Sorooshian, A.,
583 Thornhill, K. L., Voigt, C., Wan, H., Wang, H., Winstead, E., Zeng, X., Zhang, S., and Ziemba, L. D.: Aircraft
584 observations of turbulence in cloudy and cloud-free boundary layers over the western North Atlantic Ocean from
585 ACTIVATE and implications for the Earth system model evaluation and development, *Journal of Geophysical*
586 *Research: Atmospheres*, 127, e2022JD036480, <https://doi.org/10.1029/2022JD036480>, 2022.
- 587 Corral, A.F., Dadashazar, H., Stahl, C., Edwards, E.-L., Zuidema, P., and Sorooshian, A.: Source apportionment of
588 aerosol at a coastal site and relationships with precipitation chemistry: A case study over the southeast united
589 states, *Atmosphere*, 11, 1212, <https://doi.org/10.3390/atmos1111212>, 2020.
- 590 Corral, A. F., Braun, R. A., Cairns, B., Gorooh, V. A., Liu, H., Ma, L., Mardi, A. H., Painemal, D., Stamnes, S., van
591 Dierenhoven, B., Wang, H., Yang, Y., Zhang, B., and Sorooshian, A.: An overview of atmospheric features over
592 the western north Atlantic ocean and North American east coast – Part 1: Analysis of aerosols, gases, and wet



593 deposition chemistry, *Journal of Geophysical Research: Atmospheres*, 126, e2020JD032592,
594 <https://doi.org/10.1029/2020JD032592>, 2021.

595 Corral, A. F., Choi, Y., Collister, B. L., Crosbie, E., Dadashazar, H., DiGangi, J. P., Diskin, G. S., Fenn, M., Kirschler,
596 S., Moore, R. H., Nowak, J. B., Shook, M. A., Stahl, C. T., Shingler, T., Thornhill, K. L., Voigt, C., Ziemba, L.
597 D., and Sorooshian, A.: Dimethylamine in cloud water: a case study over the northwest Atlantic Ocean,
598 *Environmental Science: Atmospheres*, 2, 1534-1550, <https://doi.org/10.1039/d2ea00117a>, 2022.

599 Crosbie, E., Brown, M. D., Shook, M., Ziemba, L., Moore, R. H., Shingler, T., Winstead, E., Thornhill, K. L.,
600 Robinson, C., MacDonald, A. B., Dadashazar, H., Sorooshian, A., Beyersdorf, A., Eugene, A., Collett Jr, J.,
601 Straub, D., and Anderson, B.: Development and characterization of a high-efficiency, aircraft-based axial cyclone
602 cloud water collector, *Atmospheric Measurement Techniques*, 11, 5025-5048, [https://doi.org/10.5194/amt-11-](https://doi.org/10.5194/amt-11-5025-2018)
603 [5025-2018](https://doi.org/10.5194/amt-11-5025-2018), 2018.

604 Dadashazar, H., Wang, Z., Crosbie, E., Brunke, M., Zeng, X., Jonsson, H., Woods, R. K., Flagan, R. C., Seinfeld, J.
605 H., and Sorooshian, A.: Relationships between giant sea salt particles and clouds inferred from aircraft
606 physicochemical data, *Journal of Geophysical Research Atmospheres*, 122, 3421–3434,
607 <https://doi.org/10.1002/2016JD026019>, 2017.

608 Dadashazar, H., Painemal, D., Alipanah, M., Brunke, M., Chellappan, S., Corral, A. F., Crosbie, E., Kirschler, S., Liu,
609 H., Moore, R. H., Robinson, C., Scarino, A. J., Shook, M., Sinclair, K., Thornhill, K. L., Voigt, C., Wang, H.,
610 Winstead, E., Zeng, X., Ziemba, L., Zuidema, P., and Sorooshian, A.: Cloud drop number concentrations over the
611 western North Atlantic Ocean: seasonal cycle, aerosol interrelationships, and other influential factors,
612 *Atmospheric Chemistry and Physics*, 21, 10499-10526, <https://doi.org/10.5194/acp-21-10499-2021>, 2021.

613 Dadashazar, H., Corral, A. F., Crosbie, E., Dmitrovic, S., Kirschler, S., McCauley, K., Moore, R., Robinson, C.,
614 Schlosser, J. S., Shook, M., Thornhill, K. L., Voigt, C., Winstead, E., Ziemba, L., and Sorooshian, A.: Organic
615 enrichment in droplet residual particles relative to out of cloud over the northwestern Atlantic: analysis of airborne
616 ACTIVATE data, *Atmospheric Chemistry and Physics*, 22, 13897-13913, [https://doi.org/10.5194/acp-22-13897-](https://doi.org/10.5194/acp-22-13897-2022)
617 [2022](https://doi.org/10.5194/acp-22-13897-2022), 2022a

618 Dadashazar, H.; Crosbie, E.; Choi, Y.; Corral, A.F.; DiGangi, J.P.; Diskin, G.S.; Dmitrovic, S.; Kirschler, S.; McCauley,
619 K.; Moore, R.H.; et al.: Analysis of MONARC and ACTIVATE airborne aerosol data for aerosol-cloud interaction
620 investigations: Efficacy of stairstepping flight legs for airborne in situ sampling, *Atmosphere*, 13, 1242,
621 <https://doi.org/10.3390/atmos13081242>, 2022b.

622 Diskin, G., Podolske, J., Sachse, G., and Slate, T.: Open-path airborne tunable diode laser hygrometer. *Society of*
623 *Photo-Optical Instrumentation Engineers*, 4817, <https://doi.org/10.1117/12.453736>, 2002.

624 Dong, X., Schwantes, A. C., Xi, B., and Wu, P.: Investigation of the marine boundary layer cloud and CCN properties
625 under coupled and decoupled conditions over the Azores, *Journal of Geophysical Research: Atmospheres*, 120,
626 6179-6191, <https://doi.org/10.1002/2014JD022939>, 2015.

627 Edwards, E. L., Choi, Y., Crosbie, E. C., DiGangi, J. P., Diskin, G. S., Robinson, C. E., Shook, M. A., Winstead, E. L.,
628 Ziemba, L. D., and Sorooshian, A.: Sea-salt reactivity over the northwest Atlantic: an in-depth look using the



- 629 airborne ACTIVATE dataset, *Atmospheric Chemistry and Physics*, 24, 3349-3378, 10.5194/acp-24-3349-2024,
630 2024.
- 631 Froyd, K. D., Murphy, D. M., Brock, C. A., Campuzano-Jost, P., Dibb, J. E., Jimenez, J. L., Kupc, A., Middlebrook,
632 A. M., Schill, G. P., Thornhill, K. L., Williamson, C. J., Wilson, J. C., and Ziemba, L. D.: A new method to
633 quantify mineral dust and other aerosol species from aircraft platforms using single-particle mass spectrometry.
634 *Atmospheric Measurement Techniques*, 12, 11, 6209-6239, <https://doi.org/10.5194/amt-12-6209-2019>, 2019.
- 635 Gonzalez, M. E., Corral, A. F., Crosbie, E., Dadashazar, H., Diskin, G. S., Edwards, E.-L., Kirschler, S., Moore, R.
636 H., Robinson, C. E., Schlosser, J. S., Shook, M., Stahl, C., Thornhill, K. L., Voigt, C., Winstead, E., Ziemba, L.
637 D., and Sorooshian, A.: Relationships between supermicrometer particle concentrations and cloud water sea-salt
638 and dust concentrations: analysis of MONARC and ACTIVATE data, *Environmental Science: Atmospheres*, 2,
639 738-752, <https://doi.org/10.1039/D2EA00049K>, 2022.
- 640 Goren, T., Rosenfeld, D., Sourdeval, O., and Quaas, J.: Satellite observations of precipitating marine stratocumulus
641 show greater cloud fraction for decoupled clouds in comparison to coupled clouds, *Geophysical Research Letters*,
642 45, 5126-5134, <https://doi.org/10.1029/2018GL078122>, 2018.
- 643 Griesche, H. J., Ohneiser, K., Seifert, P., Radenz, M., Engelmann, R., and Ansmann, A.: Contrasting ice formation in
644 Arctic clouds: surface-coupled vs. surface-decoupled clouds, *Atmospheric Chemistry and Physics*, 21, 10357-
645 10374, <https://doi.org/10.5194/acp-21-10357-2021>, 2021.
- 646 Hilario, M. R. A., Crosbie, E., Bañaga, P. A., Betito, G., Braun, R. A., Cambaliza, M. O., Corral, A. F., Cruz, M. T.,
647 Dibb, J. E., Lorenzo, G. R., MacDonald, A. B., Robinson, C. E., Shook, M. A., Simpas, J. B., Stahl, C., Winstead,
648 E., Ziemba, L. D., and Sorooshian, A.: Particulate oxalate-to-sulfate ratio as an aqueous processing marker:
649 Similarity across field campaigns and limitations, *Geophysical Research Letters*, 48, e2021GL096520,
650 <https://doi.org/10.1029/2021GL096520>, 2021.
- 651 Jones, C. R., Bretherton, C. S., and Leon, D.: Coupled vs. decoupled boundary layers in VOCALS-REx, *Atmospheric*
652 *Chemistry and Physics*, 11, 7143-7153, <https://doi.org/10.5194/acp-11-7143-2011>, 2011.
- 653 Kirschler, S., Voigt, C., Anderson, B., Campos Braga, R., Chen, G., Corral, A. F., Crosbie, E., Dadashazar, H., Ferrare,
654 R. A., Hahn, V., Hendricks, J., Kaufmann, S., Moore, R., Pöhlker, M. L., Robinson, C., Scarino, A. J.,
655 Schollmayer, D., Shook, M. A., Thornhill, K. L., Winstead, E., Ziemba, L. D., and Sorooshian, A.: Seasonal
656 updraft speeds change cloud droplet number concentrations in low-level clouds over the western North Atlantic.
657 *Atmospheric Chemistry and Physics*, 22, 12, 8299-8319, <https://doi.org/10.5194/acp-22-8299-2022>, 2022.
- 658 Kirschler, S., Voigt, C., Anderson, B. E., Chen, G., Crosbie, E. C., Ferrare, R. A., Hahn, V., Hair, J. W., Kaufmann, S.,
659 Moore, R. H., Painemal, D., Robinson, C. E., Sanchez, K. J., Scarino, A. J., Shingler, T. J., Shook, M. A.,
660 Thornhill, K. L., Winstead, E. L., Ziemba, L. D., and Sorooshian, A.: Overview and statistical analysis of
661 boundary layer clouds and precipitation over the western North-Atlantic Ocean. *EGUsphere*, 1-29.
662 <https://doi.org/10.5194/egusphere-2023-898>, 2023.
- 663 Korhonen, H., Carslaw, K. S., Spracklen, D. V., Mann, G. W., and Woodhouse, M. T.: Influence of oceanic dimethyl
664 sulfide emissions on cloud condensation nuclei concentrations and seasonality over the remote Southern



- 665 Hemisphere oceans: A global model study, *Journal of Geophysical Research: Atmospheres*, 113,
666 <https://doi.org/10.1029/2007JD009718>, 2008.
- 667 Ma, L., Dadashazar, H., Hilario, M. R. A., Cambaliza, M. O., Lorenzo, G. R., Simpas, J. B., Nguyen, P., and
668 Sorooshian, A.: Contrasting wet deposition composition between three diverse islands and coastal North
669 American sites, *Atmospheric Environment*, 244, 117919, <https://doi.org/10.1016/j.atmosenv.2020.117919>, 2021.
- 670 MacDonald, A. B., Hossein Mardi, A., Dadashazar, H., Azadi Aghdam, M., Crosbie, E., Jonsson, H. H., Flagan, R. C.,
671 Seinfeld, J. H., and Sorooshian, A.: On the relationship between cloud water composition and cloud droplet
672 number concentration. *Atmos. Chem. Phys.*, 20, 13, 7645-7665, <https://doi.org/10.5194/acp-20-7645-2020>, 2020.
- 673 McNaughton, C. S., Clarke, A. D., Howell, S. G., Pinkerton, M., Anderson, B., Thornhill, L., Hudgins, C., Winstead,
674 E., Dibb, J. E., Scheuer, E., and Maring, H.: Results from the DC-8 Inlet Characterization Experiment (DICE):
675 Airborne versus surface sampling of mineral dust and sea-salt aerosols, *Aerosol Science and Technology*, 41, 136-
676 159, <https://doi.org/10.1080/02786820601118406>, 2007.
- 677 Nicholls, S.: The dynamics of stratocumulus: Aircraft observations and comparisons with a mixed layer model,
678 *Quarterly Journal of the Royal Meteorological Society*, 110, 783-820, <https://doi.org/10.1002/qj.49711046603>,
679 1984.
- 680 Painemal, D., Corral, A. F., Sorooshian, A., Brunke, M. A., Chellappan, S., Afzali Goroooh, V., Ham, S.-H., O'Neill,
681 L., Smith Jr., W. L., Tselioudis, G., Wang, H., Zeng, X., and Zuidema, P.: An overview of atmospheric features
682 over the western North Atlantic ocean and North American east coast—Part 2: Circulation, boundary layer, and
683 clouds, *Journal of Geophysical Research: Atmospheres*, 126, e2020JD033423,
684 <https://doi.org/10.1029/2020JD033423>, 2021.
- 685 Painemal, D., Chellappan, S., Smith Jr., W. L., Spangenberg, D., Park, J. M., Ackerman, A., Chen, J., Crosbie, E.,
686 Ferrare, R., Hair, J., Kirschler, S., Li, X.-Y., McComiskey, A., Moore, R. H., Sanchez, K., Sorooshian, A., Tornow,
687 F., Voigt, C., Wang, H., Winstead, E., Zeng, X., Ziemba, L., and Zuidema, P.: Wintertime synoptic patterns of
688 midlatitude boundary layer clouds over the western North Atlantic: Climatology and insights from in situ
689 ACTIVATE observations, *Journal of Geophysical Research: Atmospheres*, 128, e2022JD037725,
690 <https://doi.org/10.1029/2022JD037725>, 2023.
- 691 Prabhakar, G., Ervens, B., Wang, Z., Maudlin, L. C., Coggon, M. M., Jonsson, H. H., Seinfeld, J. H., and Sorooshian,
692 A.: Sources of nitrate in stratocumulus cloud water: Airborne measurements during the 2011 E-PEACE and 2013
693 NiCE studies, *Atmospheric Environment*, 97, 166-173, <https://doi.org/10.1016/j.atmosenv.2014.08.019>, 2014.
- 694 Papritz, L. and Spengler, T.: Analysis of the slope of isentropic surfaces and its tendencies over the North Atlantic,
695 *Quarterly Journal of the Royal Meteorological Society*, 141, 3226-3238, <https://doi.org/10.1002/qj.2605>, 2015.
- 696 Ramanathan, V., Cess, R. D., Harrison, E. F., Minnis, P., Barkstrom, B. R., Ahmad, E., and Hartmann, D. Cloud-
697 radiative forcing and climate: Results from the Earth Radiation Budget Experiment. *Science*, 243, 4887, 57-63,
698 <https://doi.org/doi:10.1126/science.243.4887.57>, 1989.
- 699 Seethala, C., Zuidema, P., Edson, J., Brunke, M., Chen, G., Li, X.-Y., Painemal, D., Robinson, C., Shingler, T., Shook,
700 M., Sorooshian, A., Thornhill, L., Tornow, F., Wang, H., Zeng, X., and Ziemba, L.: On assessing ERA5 and



- 701 MERRA2 representations of cold-air outbreaks across the Gulf Stream, *Geophysical Research Letters*, 48,
702 e2021GL094364, <https://doi.org/10.1029/2021GL094364>, 2021.
- 703 Shah, V., Jaeglé, L., Thornton, J. A., Lopez-Hilfiker, F. D., Lee, B. H., Schroder, J. C., Campuzano-Jost, P., Jimenez,
704 J. L., Guo, H., Sullivan, A.P., Weber, R. J., Green, J. R., Fiddler, M. N., Bililign, S., Campos, T. L., Stell, M.,
705 Weinheimer, A.J., Montzka, D. D., and Brown, S. S.: Chemical feedbacks weaken the wintertime response of
706 particulate sulfate and nitrate to emissions reductions over the eastern United States, *National Academy of*
707 *Sciences*, 115, 8110-8115, <https://doi.org/10.1073/pnas.1803295115>, 2018.
- 708 Song, X.H., Polissar, A.V. and Hopke, P.K.: Sources of fine particle composition in the northeastern US, *Atmospheric*
709 *Environment*, 35, 31, 5277-5286, [https://doi.org/10.1016/S1352-2310\(01\)00338-7](https://doi.org/10.1016/S1352-2310(01)00338-7), 2001.
- 710 Sorooshian, A., Anderson, B., Bauer, S. E., Braun, R. A., Cairns, B., Crosbie, E., Dadashazar, H., Diskin, G., Ferrare,
711 R., Flagan, R. C., Hair, J., Hostetler, C., Jonsson, H. H., Kleb, M. M., Liu, H., MacDonald, A. B., McComiskey,
712 A., Moore, R., Painemal, D., Russell, L. M., Seinfeld, J. H., Shook, M., Smith, W. L., Thornhill, K., Tselioudis,
713 G., Wang, H., Zeng, X., Zhang, B., Ziemba, L., and Zuidema, P.: Aerosol–cloud–meteorology interaction airborne
714 field investigations: Using lessons learned from the U.S. west coast in the design of ACTIVATE off the U.S. East
715 Coast, *Bulletin of the American Meteorological Society*, 100, 1511-1528, [https://doi.org/10.1175/BAMS-D-18-](https://doi.org/10.1175/BAMS-D-18-0100.1)
716 [0100.1](https://doi.org/10.1175/BAMS-D-18-0100.1), 2019.
- 717 Sorooshian, A., Alexandrov, M. D., Bell, A. D., Bennett, R., Betito, G., Burton, S. P., Buzanowicz, M. E., Cairns, B.,
718 Chemyakin, E. V., Chen, G., Choi, Y., Collister, B. L., Cook, A. L., Corral, A. F., Crosbie, E. C., van Diedenhoven,
719 B., DiGangi, J. P., Diskin, G. S., Dmitrovic, S., Edwards, E. L., Fenn, M. A., Ferrare, R. A., van Gilst, D., Hair, J.
720 W., Harper, D. B., Hilario, M. R. A., Hostetler, C. A., Jester, N., Jones, M., Kirschler, S., Kleb, M. M., Kusterer,
721 J. M., Leavor, S., Lee, J. W., Liu, H., McCauley, K., Moore, R. H., Nied, J., Notari, A., Nowak, J. B., Painemal,
722 D., Phillips, K. E., Robinson, C. E., Scarino, A. J., Schlosser, J. S., Seaman, S. T., Seethala, C., Shingler, T. J.,
723 Shook, M. A., Sinclair, K. A., Smith Jr, W. L., Spangenberg, D. A., Stammes, S. A., Thornhill, K. L., Voigt, C.,
724 Vömel, H., Wasilewski, A. P., Wang, H., Winstead, E. L., Zeider, K., Zeng, X., Zhang, B., Ziemba, L. D., and
725 Zuidema, P.: Spatially coordinated airborne data and complementary products for aerosol, gas, cloud, and
726 meteorological studies: the NASA ACTIVATE dataset, *Earth Syst. Sci. Data*, 15, 3419-3472,
727 <https://doi.org/10.5194/essd-15-3419-2023>, 2023.
- 728 Stahl, C., Cruz, M. T., Bañaga, P. A., Betito, G., Braun, R. A., Aghdam, M. A., Cambaliza, M. O., Lorenzo, G. R.,
729 MacDonald, A. B., Hilario, M. R. A., Pabroa, P. C., Yee, J. R., Simpás, J. B., and Sorooshian, A.: Sources and
730 characteristics of size-resolved particulate organic acids and methanesulfonate in a coastal megacity: Manila,
731 Philippines, *Atmospheric Chemistry and Physics*, 20, 15907-15935, <https://doi.org/10.5194/acp-20-15907-2020>,
732 2020.
- 733
- 734 Stevens, B., Cotton, W. R., Feingold, G., and Moeng, C.-H.: Large-eddy simulations of strongly precipitating, shallow,
735 stratocumulus-topped boundary layers, *Journal of the Atmospheric Sciences*, 55, 3616-3638,
736 [https://doi.org/10.1175/1520-0469\(1998\)055<3616:LESOSP>2.0.CO;2](https://doi.org/10.1175/1520-0469(1998)055<3616:LESOSP>2.0.CO;2), 1998.



- 737 Su, T., Zheng, Y., and Li, Z.: Methodology to determine the coupling of continental clouds with surface and boundary
738 layer height under cloudy conditions from lidar and meteorological data, *Atmos. Chem. Phys.*, 22, 1453-1466,
739 <https://doi.org/10.5194/acp-22-1453-2022>, 2022.
- 740 Thornhill, K. L., Anderson, B. E., Barrick, J. D. W., Bagwell, D. R., Friesen, R., and Lenschow, D. H.: Air motion
741 intercomparison flights during Transport and Chemical Evolution in the Pacific (TRACE-P)/ACE-ASIA. *Journal*
742 *of Geophysical Research: Atmospheres*, 108, D20, <https://doi.org/10.1029/2002JD003108>, 2003.
- 743 Tornow, F., Ackerman, A. S., Fridlind, A. M., Cairns, B., Crosbie, E. C., Kirschler, S., Moore, R. H., Painemal, D.,
744 Robinson, C. E., Seethala, C., Shook, M. A., Voigt, C., Winstead, E. L., Ziemba, L. D., Zuidema, P., and
745 Sorooshian, A.: Dilution of boundary layer cloud condensation nucleus concentrations by free tropospheric
746 entrainment during marine cold air outbreaks. *Geophysical Research Letters*, 49, e2022GL098444,
747 <https://doi.org/10.1029/2022GL098444>, 2022.
- 748 Twomey, S.: Pollution and the planetary albedo, *Atmospheric Environment* (1967), 8, 1251-1256,
749 [https://doi.org/10.1016/0004-6981\(74\)90004-3](https://doi.org/10.1016/0004-6981(74)90004-3), 1974.
- 750 Wang, Z., Mora Ramirez, M., Dadashazar, H., MacDonald, A. B., Crosbie, E., Bates, K. H., Coggon, M. M., Craven,
751 J. S., Lynch, P., Campbell, J. R., Azadi Aghdam, M., Woods, R. K., Jonsson, H., Flagan, R. C., Seinfeld, J. H.,
752 and Sorooshian, A.: Contrasting cloud composition between coupled and decoupled marine boundary layer
753 clouds, *Journal of Geophysical Research: Atmospheres*, 121, 11,679-611,691,
754 <https://doi.org/10.1002/2016JD025695>, 2016.
- 755 Warren, S.G., Hahn, C.J., London, J., Chervin, R.M., Jenne, R.L.: Global distribution of total cloud cover and cloud
756 type amounts over the ocean. *United States: n. p.*, <https://doi.org/10.2172/5415329>, 1988.
- 757 Ziemba, L. D., Lee Thornhill, K., Ferrare, R., Barrick, J., Beyersdorf, A. J., Chen, G., Crumeyrolle, S. N., Hair, J.,
758 Hostetler, C., Hudgins, C., Obland, M., Rogers, R., Scarino, A. J., Winstead, E. L., and Anderson, B. E.: Airborne
759 observations of aerosol extinction by in situ and remote-sensing techniques: Evaluation of particle hygroscopicity.
760 *Geophysical Research Letters*, 40, 2, 417-422, <https://doi.org/https://doi.org/10.1029/2012GL054428>, 2013.
- 761 Zuidema, P., Painemal, D., de Szoeki, S., and Fairall, C.: Stratocumulus cloud-top height estimates and their climatic
762 implications, *Journal of Climate*, 22, 4652-4666, <https://doi.org/10.1175/2009JCLI2708.1>, 2009.